Interfacial Nanobubbles' Growth at the Initial Stage of Electrocatalytic Hydrogen Evolution

Jinwen Yu
Beijing University of Chemical Technology

Kadi Hu
Beijing University of Chemical Technology   https://orcid.org/0000-0001-7685-6428

Zhengyi Zhang
Beijing University of Chemical Technology

Liang Luo
UC Los Angeles

Yiwei Liu
Beijing University of Chemical Technology

Daojin Zhou
Nanyang Technological University

Yun Kuang
Beijing University of Chemical Technology   https://orcid.org/0000-0002-2136-0350

Haijun Xu
Beijing University of Chemical Technology

Hui Li
Institute of Physics

Haohong Duan
Tsinghua University   https://orcid.org/0000-0003-3210-0068

Xiaoming Sun (✉ sunxm@mail.buct.edu.cn)
Beijing University of Chemical Technology   https://orcid.org/0000-0002-3831-6233

Article

Keywords:

Abstract

Bubble evolution in electrolysis commonly initiates from nanobubbles (NBs), and their ultrasmall size induces unique high internal pressure and consequently high anti-potential, namely, the extra overpotential, which is of great significance but still remains rather vague. Herein, we employ the in situ electrochemical surface plasmon resonance imaging method as combined with atomic force microscopy measurement to track the formation and growth of interfacial NBs during initiative hydrogen evolution reaction. We find that NBs' growth initiate from pancake shaped ones with increasing coverage and roughly pinned three-phase boundaries and increasing contact angle and height, but the coverage remains almost unchanged after reaching equilibrium state; Further increasing overpotential leads to the rise of NBs' curvature (anti-potential), as well as higher gas outflux rate, namely, higher background current. As confirmed by molecular dynamics simulation, the "pin-rise" growth mode and the quantitative influence of NBs on the electrochemical performance has been revealed.

Introduction

Electrochemical gas evolution reactions (GERs) play vital roles at the heart of energy storage and chemical production[1-4], in areas such as water splitting[5,6] and the chlor-alkali[7] industry. For a typical process, it is widely acknowledged that the generated gas products evolve from nanobubbles (NBs) on defects (e.g., cracks or crevices) at the electrode surface, which then grow in size (commonly > 20 μm) until the buoyancy force peels them off from the electrode[8]. To lower the overpotential, which is the key to determine the device's energy efficiency, tremendous efforts have been devoted to developing catalysts with higher intrinsic activity[9-13]. Meanwhile, electrode structure engineering (e.g., nanoarray-based superaerophobic electrodes), has recently attracted attention, due to its potential for enhancing the current density per overpotential voltage[14]. This is because the interfacial bubbles formed during the GERs can block the contact between electrolytes and electrode surfaces, thereby hinder the mass transfer and system conductivity, leading to a decrease in energy efficiency[15,16].

However, different from macroscopic bubbles, the interfacial NBs would bring unexpected impacts on the electrochemical overpotential. According to the Young-Laplace equation ($\Delta p = {2\gamma}/{r}$, γ: surface tension; r: bubble radius), the internal pressure of bubbles is inversely proportional to their radius, indicating that the ultra-small size of the initiative NBs would adopt extremely high internal pressure (e.g., ~ 28 bars for 50 nm NBs)[17]. In this context, one can deduce that the increase of bubble size (radius) during the growth of NBs would lower internal pressure and consequent chemical potential of NBs[18]. In other words, after overcoming the rate-determining nucleation step, the further growth of NBs should be a smooth, fast and even accelerated process. However, practically, higher overpotential is required to overcome the initiation stage with NBs' formation, as evidenced by the monotonic increase of current density with overpotential in polarization curves. That is, how the NBs form/grow and affect the overpotential still remains a mystery.

As is well known, the behaviors of interfacial NBs exhibit strong divergence as compared with macrobubbles, owing to their ultrasmall size, optical transparency, and fast dynamics[19–22]. In pioneering studies, White *et al.* investigated the nucleation of single embryo NBs by recording the variation of current based on individual nanosized model electrodes, gaining insights into the NB's critical nuclei size, reaction rate and activation energy, supersaturation in solution, etc[23–26]. Yet, to overcome the limitation of sampling time and statistics of classic atomic force microscopy (AFM) technology[27,28], some in-situ optical imaging technologies such as total internal reflection fluorescence microscopy (TIRFM)[29] and dark field microscopy (DFM)[30] have been developed to track the evolution dynamics of NBs[29,30], demonstrating the huge potential for in-situ observation. However, more details on the NBs' growth, such as geometry (e.g., radius, height, contact angle, and curvature) and the surface coverage of electrodes, need operando detection to bridge the relationship between bubble behaviors and the electrochemical reactions with sufficient spatial and temporal resolution, as well as statistical accuracy.

In this study, a surface plasmon resonance imaging (SPRi) technique, which is extremely sensitive to the dielectric field change, and widely used in biological binding/recognition studies[31–33], is employed to investigate the formation and growth of interfacial NBs using the hydrogen evolution reaction (HER) as a probe. An operando real-time observation system is set up with Pt/Au nano-film as both working electrode and plasmonic imaging platform, where the SPRi reveals the growth of NBs statistically by showing the increased reflectivity, and AFM yields images with high spatial definition (*e.g.*, pinning states and curvatures). It is observed that NBs initiate from pancake shaped ones, and then inflate with pinned three-phase boundaries, leading to the increased bubble contact angle (CA) and height, reduced curvature radius, and higher chemical potential of gas inside the NBs. Such higher chemical potential results in higher supersaturation of vicinal dissolved gas and a greater background current, as a consequence of increased overpotentials. And this process is further confirmed by molecular dynamics (MD) simulation.

Results

We conducted HER using Pt deposited Au film with mild hydrophilicity (CA = 56°) as the working electrode. Similar to those typical polarization curves, the overpotential losses can be divided into three parts[34–36] (Fig. 1A): activation overpotential (η_a)[15,37], ohmic overpotential (η_{ohm})[38,39], and concentration overpotential (η_{conc})[35,40–41]. However, as the electrode surface was treated by oxygen plasma to strengthen the hydrophilicity till water droplet CA drop to 12° (Fig. 1A inset), an obvious extra HER overpotential, ~ 100 mV as compared with the electrode without oxygen plasma treatment, emerged, which we define as η_i, the overpotential at initial stage of gas evolution reactions. By contrast, as the reaction switched to the no-bubble redox of potassium ferricyanide on the two identical electrodes with/without the oxygen plasma treatment, the two reduction curves overlap perfectly (Fig. 1B and Supplementary Fig. 1), indicating the extra overpotential (η_i) should be related to the new (gas) phase formation.

Increasing overpotentials from 50 mV to 200 mV (*vs* RHE) with an interval of 50 mV were applied on oxygen plasma treated Pt/Au electrode to check the bubble-effect. As shown in Fig. 1C, there are no visible bubbles on the electrode surface under small overpotentials (50 and 100 mV). During this period, the current density remains low (≤ 1 mA/cm^2, the blue dots in Fig. 1A corresponds to the blue panel in Fig. 1C). The current ramps up exponentially only when the overpotential is sufficiently high (*e.g.,* 150 mV) and visible bubbles start to emerge on the electrodes. With the further increase of the overpotential (*e.g.,* 200 mV), more macroscopic bubbles are generated on the electrode, whose growing and detaching induce strong current fluctuations (orange panel in Fig. 1C, and the organic dot in Fig. 1A).

The above "current fading" experimental phenomena should be relative to the NBs formation at the electrode/electrolyte interface before the appearance of macrobubbles under a relative large potential window (nearly 100 mV) after the oxygen plasma treatment[42]. To get further deep insights into the interface behaviors of electrode/electrolyte, SPRi technology, a method with high sensitivity to dielectric constant change at the nanoscale[43−46], was applied to investigate the "invisible" NBs at the surface of Pt/Au prism electrode after careful verification (Supplementary Fig. 2). And, the applied overpotentials are restricted to lower than 100 mV to avoid visible bubbles' formation.

The experimental setup of the electrochemical SPR (EC-SPR) was established based on the Kretschmann configuration[47] to explore the behaviors of NBs (Fig. 2A). The polarized incident light (808 nm) was directed onto the Pt/Au film via a BK7 quartz prism, and the reflected light was imaged with the objective. At the same time, a SPR response (variation of reflectivity) from the totally inner reflected light was obtained. Since the reflectivity is highly dependent on the dielectric constant, as a new gas phase forms, namely, the evolution of bubbles, there would be considerable dielectric constant change, and the reflectivity change can thus indicate the bubble-coverage ratio. The control experiment was conducted with a certain area totally covered by a planted macrobubble, and the reflectivity can reach up to the maximum value of ~ 36%, which is also in accord with the theoretical calculation (Supplementary 3), which is much higher than that of totally covered by the common applied DNA molecules (7%). Therefore, the variation of reflectivity of SPR of generated NBs from the totally inner reflected light can be regarded as a bubble-coverage ratio.

After the oxygen plasma treatment of electrode, as conducted at the overpotential of 30 mV (-30 mV *vs* R.H.E. electrode) with the scanning rate of 5.0 mV·s^{-1} in a 0.05 M H$_2$SO$_4$ solution, the current density rapidly decreases in 5 min and gradually reaches to a plateau after 20 min (Fig. 2B), accompanied by the brightening of typical SPR images of the whole prism (Fig. 2C), as well as a fast increase of reflectivity reaching up to ~ 3%, which implies the formation of NBs with the coverage of nearly 8% on the electrode (100% * 3% / 36%).

Since the SPR imaging has a lateral resolution at mainly micrometer scale, we performed an *in-situ* time-dependent AFM test on a hydrophilic electrode within a 10·10 µm^2 area under the same reaction conditions (Fig. 2D) to source the time-dependence function of the current density and the reflectivity. Profile details of each NB, including the height, the contact area can be obtained by AFM after tip-

correction, which was conducted by scanning a standard substrate with given size (280 x 200 nm^2), and the clear image verifies the tip precision (Supplementary Fig. 4). Before the reaction, the roughness of the Pt/Au surface was verified as low as 1.3 nm (Supplementary Fig. 5). At the very beginning of the reaction (~ 1 min), there are a few tiny white spots accounting for only 0.4% coverage (the ratio of the total contact area of NBs to the electrode area.) in the whole area, which are further confirmed as NBs by showing negative signal in the force profile (dim spots in Supplementary Fig. 6). As the working time prolongs from 1 to 30 min, the coverage of NBs increases from 0.4–8.2%, as evidenced by the 3D-view AFM images (Fig. 2E), with some NB agglomerates (Supplementary Fig. 7). The evolution of NBs' coverage, varying from fast increase to plateau, matches well with the variation of current density and the reflectivity of SPR images (Supplementary Fig. 8). Accompanied by the continuous formation of NBs on the electrode surface, the current density reaches an equilibrium value of 0.083 mA cm^{-2}.

As the overpotential is proportional to the driving force for the growth of NBs, various overpotentials (10 mV to 50 mV) of HER were applied to induce variations of current density and SPR reflectivity (Fig. 3A and B). As conducted at the overpotential of 10 mV for 10 min, the system tends to approach dynamic equilibrium state with the current density of 0.047 mA cm^{-2} and the reflectivity of 1.4% after the initial rapid decrease of current density and increase of reflectivity. As the applied overpotential increases, both the current density and the reflectivity rapidly reach to corresponding new plateaus (current density plateaus of 0.050 to 0.069, 0.095, and 0.157 mA cm^{-2}, corresponding to the given overpotentials of 20, 30, 40, and 50 mV, respectively). Accordingly, the reflectivity exhibits the same rising trend (from 1.5–1.7%, 2.0%, and 2.7%) as the current density (Fig. 3C). This indicates that each overpotential can supply certain driving force to form NBs with given curvature, and enable a new balanced state with an equilibrium current density. After normalizing the time-dependent current variations (Supplementary Fig. 9), it can be found that the current density reaches equilibrium with essentially the same time at different overpotentials, as well as the changing trend of current (Supplementary Fig. 10). Correspondingly, the brightness of SPR images of the equilibrium states also rise faster with the increase of overpotential but terminate at the same time point (Fig. 3D). As revealed by the top-view and 3D-view of the AFM measurement (Fig. 3E, F), the coverage of equilibrium NBs surprisingly maintains nearly constant as 7% ±1% under different overpotentials, besides more agglomerates appear under higher overpotentials (e.g. -50 mV), which indicates that the brightening of SPR images would be mainly attributed to the variation of NB morphology/height.

In the SPR configuration, the excited evanescent wave usually propagates tens of micrometers in lateral direction, thus the reflectivity is sensitive to the interfacial variation. As there are species adsorbed or generated on the given surface, the localized evanescent wave would be greatly attenuated and the reflectivity would increase. By contrast, in vertical direction, the evanescent wave is exponentially damped as away from the interface (Supplementary Fig. 11A), so that the reflectivity is not sensitive to the height of NBs, excepted for the bubble edge. For the cap-shaped surface NBs, their edge region is with rather small height, usually lower than 10 nm, and the edge part of evanescent wave would be partially attenuated, not as fully as the central part (Supplementary Fig. 11B). As a result, when interfacial NBs

further grow with the increase of contact angle, the edge part would be thickened, and the corresponding localized evanescent wave would be further attenuated slightly, leading to a limited increase of reflectivity (Supplementary Fig. 11C).

Deep analysis of the AFM measurements was applied to get more detailed structural parameters of NBs to reveal how the SPR images get brighter under the same bubble coverage. As shown in Fig. 4A and 4B, with the height (H) and the contact diameter (D), the curvature radius (r) of the NBs can be calculated from the equation $r = \frac{H^2 + D^2/4}{2H}$, and thereby the bubble CA can also be obtained. Typically, under a constant overpotential of 30 mV, a few embryo NBs nucleate stochastically on the electrode surface within 1 min, as an initial pinning state with an average CA of $\sim$ 26° (H=7 nm, D=62 nm, and r=74 nm, corresponding to 19.5 bar). Subsequently, massive NBs form in the next 5 min, and the size and shape of NBs also change rapidly to reach CA of $\sim$ 45° (H=13 nm, D=72 nm, and r=51.5 nm, corresponding to 28 bar). As the reaction time is extended to 30 min, the coverage of NBs approaches the constant value of 8.2% (Fig. 2D), and the morphology also stabilize (CA=47°, H=15 nm, D=74 nm, and r=51.5 nm, corresponding to 28 bar), indicating the dynamic equilibrium state. The analyses indicate that at a given overpotential higher than that required for NB nucleation, the interfacial NBs grow rapidly with fast increasing CA (from 26° to 45°), H (from 7 to 15 nm), but limited change of D (from 62 to 74 nm). Namely, the three-phase boundaries move outward a little within the first 8 min, then reach to a dynamic equilibrium state with constant morphology and pinning contact lines. While the curvature indicator, r, decreases rapidly at first and approaches to a plateau at last (from 74 to 51.5 nm) as evidenced by the time-dependent statistics of AFM measurement (Supplementary Fig. 12). It should be noted that the constant contact diameter (CCD) mode is also nearly applicable to describe the NBs growth features, where the diameter only expends from 62 nm to 72 nm (16%) while the height is increased from 7 nm to 13 nm (nearly 2 times). It is also closely related to the "rising-up" growth mode, which bridges the growth behaviors of NBs and the impact on overpotential, based on the well-known characteristic CCD mode.

According to the statistics of the NBs' dynamic equilibrium states under different overpotentials from 10 to 50 mV (Supplementary Figs. 13 and 14), the average values of CA gradually increase from 40° to 65°, and H simultaneously climbs from 10 to 19 nm, while D only slightly varies from 64 to 68 nm. This indicates a stricter, nearly CCD variation mode of the NBs with their three-phase boundaries steadily pinning on the surface (Fig. 4C and D) than the time-extension case. Such CCD evolution mode leads to a decrease of r from 56 to 40 nm; Correspondingly, the internal pressure of NBs would be increased by $\sim$ 40% according to Laplace pressure calculation. It explains the reason why the initiative η_i is much more obvious after oxygen plasma treatment: the plasma treated Pt/Au surface is of higher hydrophilicity, which means the extension of bubbles' zones or movement of the contact line into liquid phase would be more difficult (Fig. 1A). As surface confirmed by the variations of the SPR images and the curves with different oxygen plasma treatment time, NBs are more likely to be retained on the electrode surface with higher hydrophilicity (aerophobicity) (Supplementary Fig. 15).

Moreover, it is further found that the change in coverage is rather limited (< 1.5%) at various overpotential (10−50 mV, Supplementary Fig. 16), and the number density (ρ) of NBs is almost unchanged (Fig. 4B and 4D), indicating that the increased overpotential prefers to promote the "pin-rise" growth of formed NBs rather than the new bubble nucleation. As a result, the reflectivity variation and the brightening of the SPR images (Fig. 3B and 3D) under different overpotentials can be mostly attributed to the increase of bubbles' height, as the evanescent wave on Pt/Au surface can be extended to the height of ∼ 200 nm based on the applied polarized incident laser of 808 nm in principles (Supplementary Fig. 11A)[48]. The results reveal that the equilibrated geometry of formed interfacial NBs tightly depends the applied overpotential: the higher applied overpotential causes the higher chemical potential of the electrochemically generated gas, corresponding to the higher internal pressure of the raised interfacial NBs (with smaller curvature radius).

Since the operando electrochemical cell in our experiments can be regarded as an open system without sealing, the high pressure inside NBs (26−36 bar) would lead to supersaturated environments which release H_2 into the bulk solution besides into bubbles. Thus, the decrease of r value at higher overpotential would increase the concentration gradient between the interfacial NBs and the bulk aqueous phase, thereby enhance the outflux of H_2 from NBs to the bulk phase, to generate overpotential-dependent residual current (Fig. 3A and Supplementary Fig. 17). When the applied potential is further increased over the threshold, the overhigh internal pressure caused by the greater CA will eventually cause the sudden expansion of the three-phase contact line (i.e. de-pinning), which breaks the dynamic equilibrium between the chemical potential of NBs and the applied overpotential (and residual current). The depinning is accompanied by a sudden increase of the bubble radius and significant decrease of the gas chemical potential, leading to accelerated generation of massive amounts of gas and rapid extension of NBs and formation of macroscopic bubbles.

To uncover the molecular mechanism of surface pinning effect in NBs growth on a flat electrode surface during the GERs, as well as the corresponding relation between NB geometry and the overpotential, atomistic molecular dynamics (MD) simulations are carried out to investigate the interfacial NB formation process using an algorithm to mimic the driving force (analogous to the electrochemical overpotential) with the frequency F of gas creation attempts[49−51]. The whole simulation system is divided into three regions: the empty reservoir, the electrolyte layer, and the substrate with a cylindrical hydrophobic region (bubble-generation region) with weaker interaction parameters, as well as the surrounding hydrophilic region with stronger interaction parameters[50,52]. After the full relaxation of the whole system without any gas molecules, we start the generation of H_2 molecules by applying a certain driving force $F = 0.4$ ps^{-1} (one reaction attempts every 2.5 ps), and the formation process of the NB is shown in Fig. 5A. In agreement with the experimental observation that the initial nucleation of interfacial NBs is easy, the MD simulation shows a rapid nucleation of NB on the hydrophobic region of electrode, where the dissolved H_2 molecules tend to gather on the surface and show pancake morphology. Then, the initial growth of NB follows a triple-line-extension mode with a super large CA until the pancake gradually occupy the whole hydrophobic area of the electrode. After that, the contact line of NB is pinned by the

hydrophobic/hydrophilic boundary, and the growth of NB starts to follow a CCD mode, with the CA and the bubble height being gradually increased by the continuous injection of H_2 molecules. Meanwhile, accompanied by the increase of CA, the growth rate of NB becomes lower and gradually approaches to 0, and finally stops with a CA closed to 90° [53], which is almost the same degree on different sized substrates (Supplementary Fig. 18). By comparing the CAs and curvature radii with different driving forces (Fig. 5B and C), it is confirmed that the equilibrate CA and the curvature radius of the pinned NB are respectively increased with the increase of driving force (applied overpotential). Furthermore, the higher internal pressure of NBs under higher overpotentials is also confirmed by the MD simulation (Supplementary Fig. 19). Therefore, the simulated growth process of NBs is consistent with the experimental observations as well as previous predictions[54].

Based on the experiments and simulations, a time-dependent bubble-current model is proposed to quantify the relation between the residue current and NBs' morphology and coverage (Fig. 5D). For a typical process at a certain overpotential, the total current is generated on the electrode surface exposed to electrolyte (i_s), and also the outflux from NBs.

$$i = i_{NB} + I_s \quad (1)$$

There is no NB formed on the electrode at the very beginning (t_0), so the contribution to the current i (blue line) is solely the exposed electrode substrate is (green line). It decreases as NBs form and anti-potential works. Meanwhile, a supersaturated gradient (Fig. 5E) would form nearby the surface of each NB. The supersaturated gradients nearby NBs would release H_2 molecules into the bulk solution (the outflux of H_2). To maintain the dynamic equilibrium, more electrochemically generated H_2 is required to replenish such outflux diffusion loss; here we define as "i_{NB}" (red line). By assuming the same concentration gradient nearby each NB, the total outflux diffusion of H_2 molecules into the bulk solution on the whole electrode is proportional to the number (coverage) of NBs.

As more and more NBs form on electrode, i_{NB} continuously increases and reaches the plateau, the equilibrium state (t_{eq}). Accordingly, i_s decreases until it reaches zero. The equilibrium means both the NB coverage and the supersaturated gradients remain unchanged, and the final NB distribution can be approximately regarded a "close-packed" structure (Fig. 5E). According to the relative steady total coverage of ~ 7%±1% (blue line in Fig. 5F) by NBs at the equilibrium state at different overpotentials (e.g., 10–50 mv) at the initial stage (Fig. 5F), we can infer that every NB would affect the surrounding zone about 13 times of NBs themselves. In contrast to the unchanged total coverage, the NBs' profile (i.e., r) strongly depends on the applied overpotentials. Higher overpotential (η) endows the NBs with higher internal pressure as well as higher surrounding supersaturation gradients (bluer background in Fig. 5G, $V_1 < V_2$) according to the Young-Laplace equation, namely, higher outflux current i_{NB} (red line in Fig. 5F).

Discussion

In conclusion, we employ a combination of in situ SPRi, AFM, and MD simulation to investigate the nucleation and growth process of interfacial H_2 NBs' in the initiative stage of HER. A comprehensive picture of the interfacial NBs formation under the GER conditions has been revealed: the nucleation of interfacial NBs on the aerophilic sites of the electrode surface is easy (which can occur at very low overpotential), but the further growth of NBs requires a higher applied overpotential; Under a higher overpotential, the growth of NBs exhibits a CCD mode with the three-phase contact line pinned by the surface heterogeneity; The "pin-rise" evolution of the interfacial NBs leads to smaller curvature radius, higher Laplace internal pressure, and higher gas chemical potential, which brings the GER an extra overpotential η_i. As compared to the growth of NBs, the nucleation of new bubble on the hydrophilic surface is more difficult, as a result, the surface coverage of NBs under different overpotentials remains almost unchanged. When the applied potential exceeds the critical chemical potential of NBs, depinning of NBs occurs, leading to a sudden drop in gas pressure. Subsequently, the NBs rapidly expand to macrobubbles. Based on the data from operando SPRi and current measurements, we present a bubble-current model to establish the quantitative relation between the NB growth and the electrolysis current, which is a great step forward compared to the traditional Tafel current model for EGERs. The present work not only provides a promising tool to track the real-time growth of interfacial NBs, but also uncovers the crucial role of NBs in determining the efficiency and the overpotential of GERs, which sheds new insights for electrode design in electrochemistry.

Materials And Methods

Electrochemical SPR (EC-SPR) setup

Electrochemical SPR (EC-SPR) was conducted to explore the behaviors of nanobubbles, and the experimental setup was based on the Kretschmann configuration, as shown in Fig. 2A. Polarized incident light (808 nm) was directed onto the gold film via a BK7 quartz prism, and the reflected light was imaged with the objective. At the same time, an SPR response (variation of reflectivity) from the totally inner reflected light was obtained. The electrochemically deposited Pt on the surface of an Au-coated prism was used as the working electrode, a carbon rod as the counter electrode, and a saturated calomel electrode as reference electrode to fabricate a three-electrode in-situ electrochemical reaction cell. As the sensitivity of the SPR technique is highly dependent on the dielectric constant, the deposited amount of Pt should be very small to minimize the dielectric constant variation of original plasmonic Au film. As revealed by SEM (Supplementary Fig. 2B) and AFM images (Supplementary Fig. 20), there are no obvious Pt nanoparticles formed and no obvious color change after Pt deposition. The elementary mapping and onset potential comparison of linear sweep voltammetry (LSV) curves for Au (-0.1 V vs RHE) and Pt/Au (0 V vs RHE) electrodes (Supplementary Fig. 2A) verify the successful decoration of Pt on Au film. The influence of dielectric constant variation for SPR sensing with Pt and without Pt coated prisms was further evaluated by measuring the reflectivity under different potentials (-0.4 V-0.7 V) (Supplementary Fig. 21). There is a potential-dependent variation of reflectivity, which might result from the dielectric constant change induced by the modulation of free electrons of the metal film under different potentials,

but the very limited deviation between the two reflectivity curves (Au and Pt/Au) indicates that the dielectric constant remains nearly the same after the atomic level deposition of additive metals on the Au film.

Verification of the ultra-sensitivity toward gas molecules

Before the experiment, we assessed the theoretical reflectivity with polarized incident light (R_p) of gas molecules. The theoretical reflectivity change can be calculated from Eq. (2)[55],

$$R_p = |r_{012}|^2 = \left| \frac{r_{01} + r_{12}e^{2ik_{y1}d}}{1 + r_{01}r_{12}e^{2ik_{y1}d}} \right|^2$$

2

where r represents the reflection coefficient between the two layers; 0, 1, 2 represent prism, gas, and electrolyte, respectively.

The reflection coefficient (r) between two interfaces is given by Eq. (3)[55],

$$r_{ij} = \frac{\epsilon_j k_{yi} - \epsilon_i k_{yj}}{\epsilon_j k_{yi} + \epsilon_i k_{yj}}$$

3

where k is the longitudinal wave vector, and ε is the dielectric constant of different layers (y and j are quartz and Au, respectively). Here, the dielectric constant of quartz and Au are 2.25 and – 16, respectively.

Further, the k value can be calculated by Eq. (4)[55],

$$k_{yj}^2 = n_i^2 (2\pi/\lambda)^2 \left(n_j^2/n_i^2 - \sin 2\alpha \right)$$

4

where n_i and n_j are the refractive index of prism (1.515) and Au (1.48), respectively.

Accordingly, the theoretical reflectivity (R) change of gas molecules is calculated to be 36.6%, which is an extremely big value, and directly related to the sensitivity toward gas bubbles. To demonstrate the considerable reflectivity change, we compared the SPR curves of a single hydrogen bubble evolution on the Pt/Au film prism and reference biomolecules (DNA) recognition (Supplementary Fig. 3). As the bubble grows and finally fully occupies the pre-selected area as marked in a red circle (Supplementary Fig. 3 inset), the reflectivity gradually increases and reaches to a plateau as ~ 36%, while the reflectivity of similarly fully occupied DNA molecules is only about 7%. Similarly, the corresponding SPR images

(Supplementary Fig. 3 inset) also display that the contrast of the bubble contact area is much higher than the binding area of DNA molecules. This suggests that the SPRi is suitable for bubble observation.

Characterization of surface nanobubbles

SPRi (Horiba) and AFM (Bruker catalyst) were used to characterize the geometric change and growth trend of surface nanobubbles in the electrochemical gassing reaction. SPRi is very amenable for studying the nanobubble system due to its very high response degree, and the change of the nanobubble on the electrode can be judged according to the change trend of the image. AFM is a traditional instrument used to characterize nanobubbles. As shown in Supplementary Fig. 4, tip correction (The AFM probe scans a given patterned substrate and compares the obtained groove size with the standard size) was used to improve accuracy, and tapping mode is used to obtain the geometry of surface nanobubbles.

Simulation methodology

A patterned plate with 4 layers of Au was utilized as the substrate in the simulation. Au atoms of different color were assigned different interaction parameters to simulate heterogeneous nucleation as shown in Table 1[49,56-58]. The size of the whole simulation box is 14 nm×14 nm×12 nm. Molecular dynamics simulations are performed with a modified version of the open source code LAMMPS[59]. The equations of motion are integrated with the velocity Verlet algorithm with a time step of 5 fs. The temperature is set to 300 K, controlled with the Nose – Hoover thermostat with a relaxation time of 0.25 ps. The electrochemical production of gas at the electrode is mimicked by inserting gas molecules at a random position within a disk with the same area of the electrode and 2.5 Å above the Au electrode. The gas molecules can only be created if there is at least one water molecule within 4 Å of the creation point, because water is needed for the electrochemical reaction to proceed in the experiment. If that requirement is not met, a new gas creation attempt elsewhere above the electrode plane is carried out for the same configuration, up to ten trials. The frequency F of gas creation attempts is constant in each simulation.

The overpotential is obtained by the formula

$$\Delta E = RT \ln \frac{P_S}{P_0}$$

5

$$P = \frac{N k_B T}{V} + \frac{\sum_i^N r_i \bullet f_i}{dV}$$

6

where P_s is the internal pressure of nanobubble, P_0 is the partial pressure of H_2 in the bulk water, N is the number of atoms in calculation region, k_B is the Boltzmann constant, T is the temperature, d is the

dimensionality of the system, V is the volume of calculation region, r_i and f_i are the position and force vector of atom i, respectively, and the black dot indicates a dot product.

Table 1

Interaction parameters between atoms H represents the atom of a hydrogen molecule; W represents the O atom of a water molecule while the interaction parameters of the H atom in the water molecule are both 0; E the atom of electrode; A the atoms of the hydrophilic layer surrounding the electrode.

	H-H	W-W	E-E	A-A	H-E	H-A	W-E	W-A
(kcal/mol)	0.022	0.155	5.29	5.29	0.334	0.115	0.453	0.906
σ (Å)	2.683	3.169	2.951	2.951	2.817	2.817	2.937	3.292

Declarations

Data availability

All data are available in the main text or the supplementary materials.

Author contributions

L.L and X.S. designed research; J.Y., Z.Z., Y.L., L.L. and X.S. performed research; K. H. and H. L. performed the MD simulations; J.Y., Z.Z., Y.L., H.X., L.L., and X.S. analyzed data; and J.Y., W.L., K. H., L.L., H. Li., and X.S. wrote the paper. All the authors discussed the results and commented the manuscript.

Competing interests

Authors declare that they have no competing interests.

Additional information

Supplementary information is available for this paper.

References

1. Lu, Z. et al. Ultrahigh Hydrogen Evolution Performance of Under-water "Superaerophobic" MoS2 Nanostructured Electrodes. Adv. Mater. **26**, 2683–2687 (2014).

2. Li, Y. et al. Ternary NiCoP Nanosheet Arrays: An Excellent Bifunctional Catalyst for Alkaline Overall Water Splitting. Nano. Res. **9**, 2251−2259 (2016).

3. Deng, J. et al. Multiscale Structural and Electronic Control of Molybdenum Disulfide Foam for Highly Efficient Hydrogen Production. Nat. Commun. **8**, 1−8 (2017).

4. Tang, C., Wang, H.-F. & Zhang, Q. Multiscale Principles to Boost Reactivity in Gas-involving Energy Electrocatalysis. Acc. Chem. Res. **51**, 881−889 (2018).

5. Suen, N.-T. et al. Electrocatalysis for the Oxygen Evolution Reaction: Recent Development and Future Perspectives. Chem. Soc. Rev. **46**, 337−365 (2017).

6. Roger, I., Shipman, M.A. & Symes, M.D. Earth-abundant Catalysts for Electrochemical and Photoelectrochemical Water Splitting. Nat. Rev. Chem. **1**, 1−13 (2017).

7. Karlsson, R.K.B. & Cornell, A. Selectivity Between Oxygen and Chlorine Evolution in the Chlor-alkali and Chlorate Processes. Chem. Rev. **116**, 2982−3028 (2016).

8. Oguz, H.N. & Prosperetti, A. Dynamics of Bubble Growth and Detachment from a Needle. J. Fluid. Mech. **257**, 111−145 (1993).

9. Jahan, M., Liu, Z. & Loh, K.P. A Graphene Oxide and Copper-centered Metal Organic Framework Composite as a Tri-functional Catalyst for HER, OER, and ORR. Adv. Funct. Mater. **23**, 5363−5372 (2013).

10. Kibsgaard, J., Jaramillo, T.F. & Besenbacher, F. Building an Appropriate Active-site Motif into a Hydrogen-evolution Catalyst with Thiomolybdate $[Mo_3S_{13}]^{2-}$ Clusters. Nat. Chem. **6**, 248−253 (2014).

11. Mahmood, J. et al. An Efficient and pH-universal Ruthenium-based Catalyst for the Hydrogen Evolution Reaction. Nat. Nanotechnol. **12**, 441−446 (2017).

12. Reier, T., Oezaslan, M. & Strasser, P. Electrocatalytic Oxygen Evolution Reaction (OER) on Ru, Ir, and Pt Catalysts: A Comparative Study of Nanoparticles and Bulk Materials. Acs. Catal. **2**, 1765−1772 (2012).

13. Wang, D.-Y. et al. Highly Active and Stable Hybrid Catalyst of Cobalt-Doped FeS2 Nanosheets-carbon Nanotubes for Hydrogen Evolution Reaction. J. Am. Chem. Soc. **137**, 1587−1592 (2015).

14. Lu, Z. et al. Nanoarray Based "Superaerophobic" Surfaces for Gas Evolution Reaction Electrodes. Mater. Horiz. **2**, 294−298 (2015).

15. Dukovic, J. & Tobias, C.W. The Influence of Attached Bubbles on Potential Drop and Current Distribution at Gas-evolving Electrodes. J. Electrochem. Soc. **134**, 331−343 (1987).

16. Zhao, X., Ren, H. & Luo, L. Gas Bubbles in Electrochemical Gas Evolution Reactions. Langmuir. **35**, 5392−5408 (2019).

17. Oh, S.H., Han, J.G. & Kim, J.-M. Long-term Stability of Hydrogen Nanobubble Fuel. Fuel. **158**, 399−404 (2015).

18. Sun, Y. et al. Stability Theories of Nanobubbles at Solid−Liquid Interface: A Review. Colloid. Surface. A. **495**, 176−186 (2016).

19. Lohse, D. & Zhang, X. Surface Nanobubbles and Nanodroplets. Rev. Mod. Phys. **87**, 981 (2015).

20. Tan, B.H., An, H. & Ohl, C.-D. Surface Nanobubbles are Stabilized by Hydrophobic Attraction. Phys. Rev. Lett. **120**, 164502 (2018).

21. Brenner, M.P. & Lohse, D. Dynamic Equilibrium Mechanism for Surface Nanobubble Stabilization. Phys. Rev. Lett. **101**, 214505 (2008).

22. Tan, B.H., An, H. & Ohl, C. D. Stability Dynamics, and Tolerance to Undersaturation of Surface Nanobubbles. Phys. Rev. Lett. **122**, 134502 (2019).

23. Chen, Q. et al. Electrochemical Measurements of Single H_2 Nanobubble Nucleation and Stability at Pt Nanoelectrodes. J. Phys. Chem. Lett. **5**, 3539−3544 (2014).

24. Luo, L. & White, H.S. Electrogeneration of Single Nanobubbles at Sub-50-nm-radius Platinum Nanodisk Electrodes. Langmuir. **29**, 11169−11175 (2013).

25. Chen, Q. et al. Electrochemical Nucleation of Stable N_2 Nanobubbles at Pt Nanoelectrodes. J. Am. Chem. Soc. **137**, 12064−12069 (2015).

26. Edwards, M.A., White, H.S. & Ren, H. Voltammetric Determination of the Stochastic Formation Rate and Geometry of Individual H_2, N_2, and O_2 Bubble Nuclei. ACS. Nano. **13**, 6330−6340 (2019).

27. Lou, S. T. et al. Nanobubbles on Solid Surface Imaged by Atomic Force Microscopy. J. Vac. Sc. Technol. B. **18**, 2573−2575 (2000).

28. Zhang, X.H., Maeda, N. & Craig, V.S. Physical Properties of Nanobubbles on Hydrophobic Surfaces in Water and Aqueous Solutions. Langmuir. **22**, 5025−5035 (2006).

29. Hao, R. et al. Imaging Nanobubble Nucleation and Hydrogen Spillover During Electrocatalytic Water Splitting. *Proc. Natl. Acad. Sci. U.S.A.* **115**, 5878−5883 (2018).

30. Xu, S. et al. Real-time Visualization of the Single-nanoparticle Electrocatalytic Hydrogen Generation Process and Activity under Dark Field Microscopy. Anal. Chem. **92**, 9016−9023 (2020).

31. Wang, S. et al. Label-free Imaging, Detection, and Mass Measurement of Single Viruses by Surface Plasmon Resonance. *Proc. Natl. Acad. Sci. U.S.A.* **107**, 16028−16032 (2010).

32. Bolles, K.M. et al. Imaging Analysis of Carbohydrate-modified Surfaces Using ToF-SIMS and SPRi. Materials. **3**, 3948−3964 (2010).

33. Fang, S. et al. Attomole Microarray Detection of MicroRNAs by Nanoparticle-amplified SPR Imaging Measurements of Surface Polyadenylation Reactions. J. Am. Chem. Soc. **128**, 14044−14046 (2006).

34. Angulo, A. et al. Influence of Bubbles on the Energy Conversion Efficiency of Electrochemical Reactors. Joule. **4**, 555−579 (2020).

35. Newman, J. & Thomas-Alyea, K.E. Electrochemical Systems (John Wiley & Sons) (2004).

36. Leistra, J.A. & Sides, P.J. Voltage Components at Gas Evolving Electrodes. J. Electrochem. Soc. **134**, 2442−2446 (1987).

37. Vogt, H. & Balzer, R.J. The Bubble Coverage of Gas-evolving Electrodes in Stagnant Electrolytes. Electrochim. Acta. **50**, 2073−2079 (2005).

38. Eigeldinger, J. & Vogt, H. The Bubble Coverage of Gas-evolving Electrodes in a Flowing Electrolyte. Electrochim. Acta. **45**, 4449–4456 (2000).

39. Newman, J. Scaling with Ohm's law; Wired vs. Wireless Photoelectrochemical Cells. J. Electrochem. Soc. **160**, F309–F311 (2013).

40. Bard, A.J. Electrochemical Methods: Fundamentals and Applications, Educ. L.R. Faulkner (John Wiley) (2001).

41. Pande, N. et al. Correlating the Short-time Current Response of a Hydrogen Evolving Nickel Electrode to Bubble Growth. J. Electrochem. Soc. **166**, E280–E285 (2019).

42. Zhang, L. et al. Electrochemically Controlled Formation and Growth of Hydrogen Nanobubbles. Langmuir. **22**, 8109–8113 (2006).

43. Shan, X. et al. Imaging the Electrocatalytic Activity of Single Nanoparticles. Nat. Nanotechnol. **7**, 668–672 (2012).

44. Jiang, D. et al. Optical Imaging of Phase Transition and Li-ion Diffusion Kinetics of Single LiCoO2 Nanoparticles during Electrochemical Cycling. J. Am. Chem. Soc. **139**, 186–192 (2017).

45. Shan, X. et al. Imaging local electrochemical Current via Surface Plasmon Resonance. Science. **327**, 1363–1366 (2010).

46. Chen, J. et al. Measuring the Activation Energy Barrier for the Nucleation of Single Nanosized Vapor Bubbles. *Proc. Natl. Acad. Sci. U.S.A.* **116**, 12678–12683 (2019).

47. Nakamoto, K. et al. Development of a Mass-Producible On-chip Plasmonic Nanohole Array Biosensor. Nanoscale. **3**, 5067–5075 (2011).

48. Schasfoort, R.B. Handbook of Surface Plasmon Resonance (Royal Society of Chemistry) (2017).

49. Gadea, E.D. et al. Electrochemically Generated Nanobubbles: Invariance of the Current with Respect to Electrode Size and Potential. J. Phys. Chem. Lett. **11**, 6573–6579 (2020).

50. Perez Sirkin, Y.A. et al. Mechanisms of Nucleation and Stationary States of Electrochemically Generated Nanobubbles. J. Am. Chem. Soc. **141**, 10801–10811 (2019).

51. Lemay, S.G. Noise as Data: Nucleation of Electrochemically Generated Nanobubbles. ACS. Nano. **13**, 6141–6144 (2019).

52. Maheshwari, S. et al. Stability of Surface Nanobubbles: A Molecular Dynamics Study. Langmuir. 32, 11116–11122 (2016).

53. Dockar, D., Borg, M.K. & Reese, J.M. Mechanical Stability of Surface Nanobubbles. Langmuir. **35**, 9325–9333 (2018).

54. Ushikubo, F.Y. et al. Evidence of the Existence and the Stability of Nano-bubbles in Water. Colloid. Surface. A. **361**, 31–37 (2010).

55. Kim, J.Y. et al.Efficient Tandem Polymer Solar Cells Fabricated by All-solution Processing. Science. **317**, 222–225 (2007).

56. Bouanich, J. P. Site-site Lennard-Jones Potential Parameters for N_2, O_2, H_2, CO and CO_2. J. Quant. Spectrosc. RA. **47**, 243–250 (1992).

57. Berendsen, H., Grigera, J. & Straatsma, T. The Missing Term in Effective Pair Potentials. J. Phys. Chem. **91**, 6269–6271 (1987).

58. Heinz, H. et al. Accurate Simulation of Surfaces and Interfaces of Face-centered Cubic Metals Using 12 − 6 and 9 − 6 Lennard-Jones Potentials. J. Phys. Chem. C. **112**, 17281–17290 (2008).

59. Plimpton, S. Fast Parallel Algorithms for Short-range Molecular Dynamics. J. Comput. phys. **117**, 1–19 (1995).
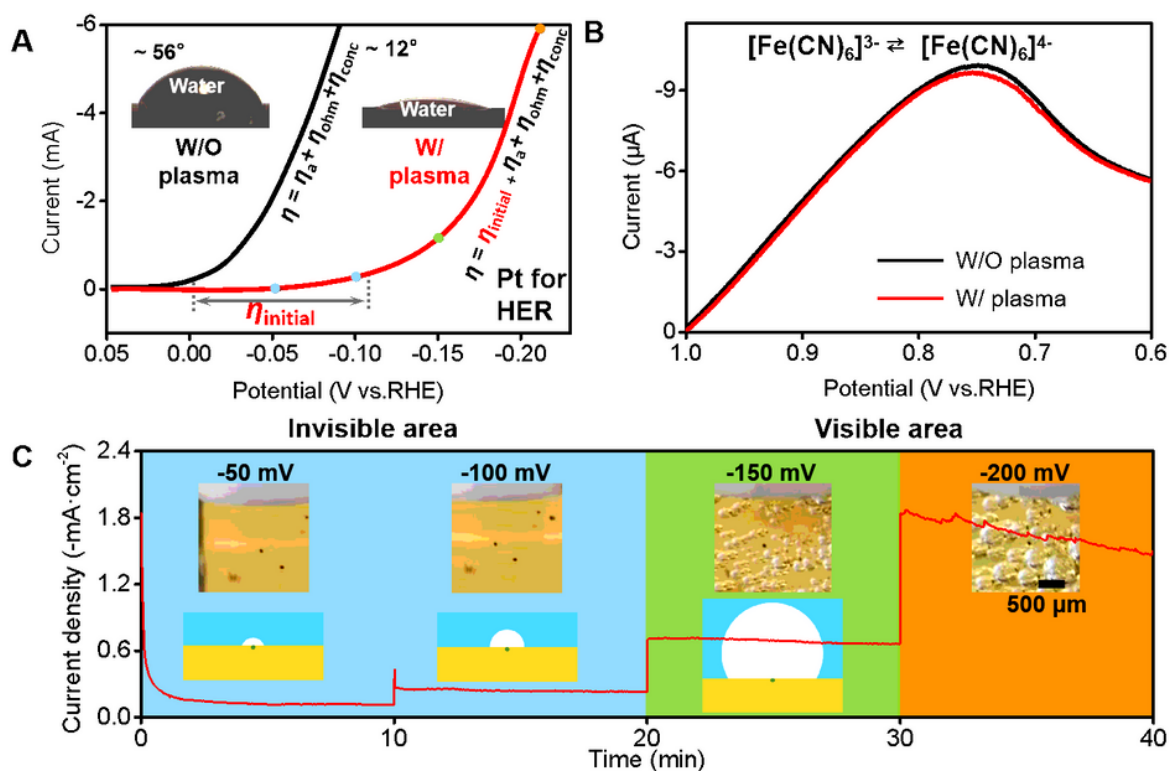
Figures

Figure 1

Hydrogen evolution reaction (HER) on an oxygen-plasma-treated Pt/Au flat electrode. (A) Linear sweep voltammetry curves (LSV) of HER with (the red line) and without (the black line) oxygen plasma treatment. An additional initial overpotential (i) emerges after plasma treatment. **(B)** The overlapping LSV oxidation curves of [Fe(CN)6]3- ↔ [Fe(CN)6]4- recorded on electrodes with (the red line) and without (the black line) oxygen plasma treatment. **(C)** Overpotential-dependent current steps before (V≤100mV) and after (V≥150mV) formation of visible bubbles, and corresponding bubbles' images on electrodes.
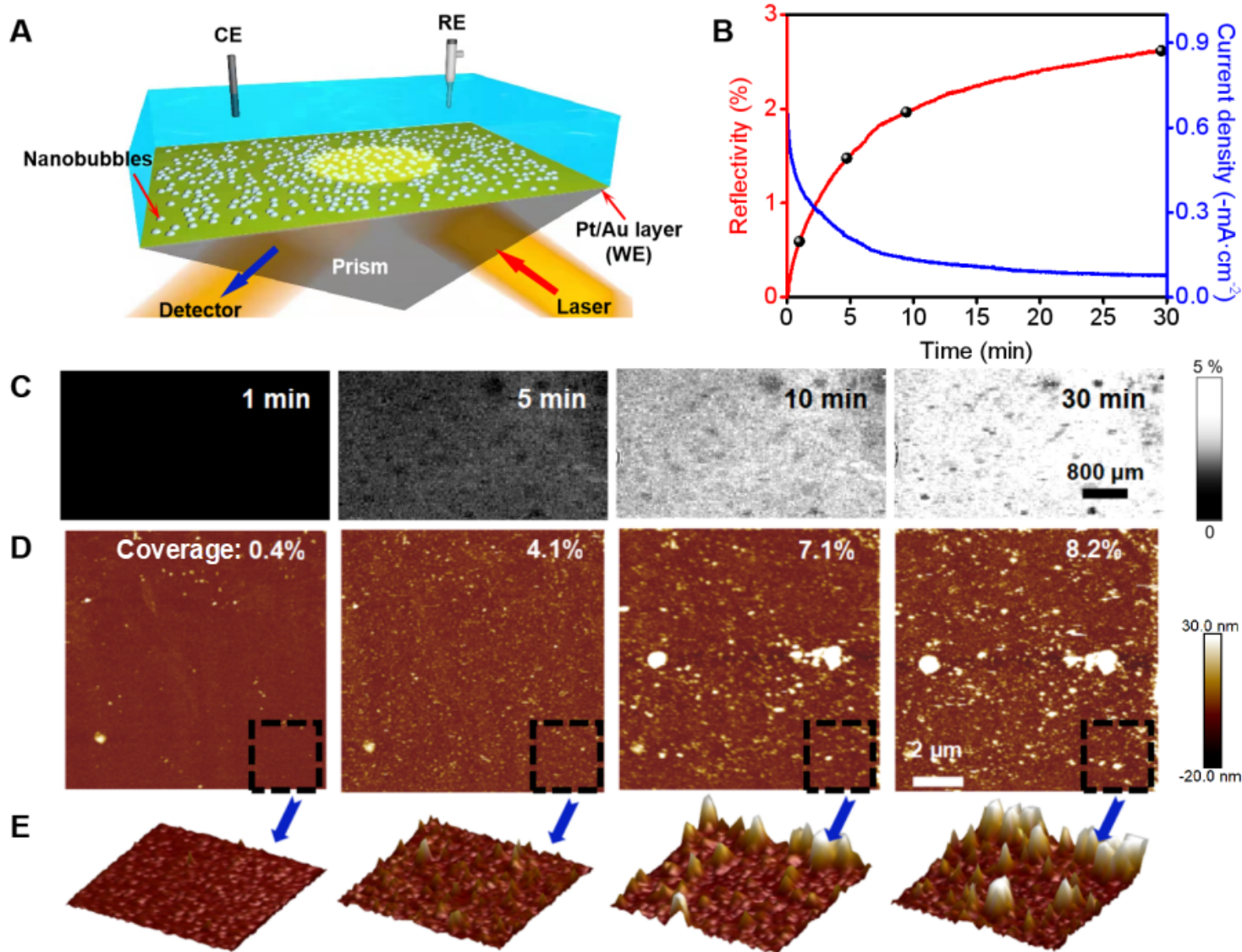
Figure 2

Time-dependent evolution of NBs at overpotential of 50 mv. (A) Schematic diagram of experimental setup for the electrochemical surface plasmon resonance imaging (EC-SPRi). **(B)** Time-dependent SPR reflectivity (red curve, left axis) and current density (blue curve, right axis). **(C)** SPR, **(D)** AFM, and **(E)** 3D views of AFM images captured at 1, 5, 10, and 30 min during hydrogen evolution reaction.
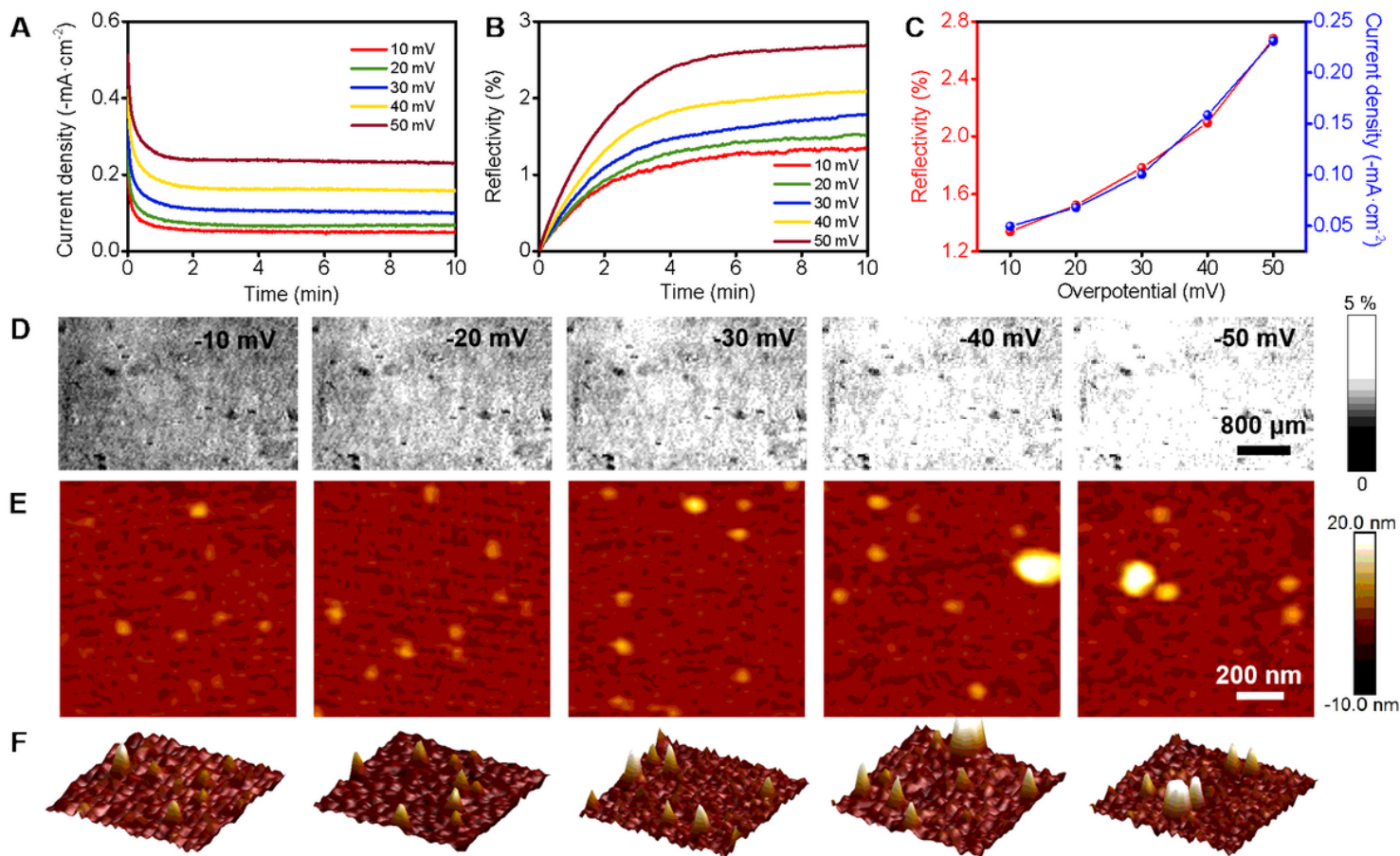
Figure 3

Overpotential-dependent variations of nanobubbles. (A) Current density, and **(B)** reflectivity of SPRi of Pt/Au electrodes, as functions of time at varied overpotentials: 10, 20, 30, 40, and 50 mV. **(C)** Curves plotting the reflectivity (red dots) and equilibrium current (blue dots) as functions of overpotential. Overlapping of the 2 lines indicates the strong relationship of the two factors. **(D)** SPR, **(E)** AFM, and **(F)** 3D-view of AFM images captured at -10, -20, -30, -40 and -50 mV during HER at plateau zone of SPR.
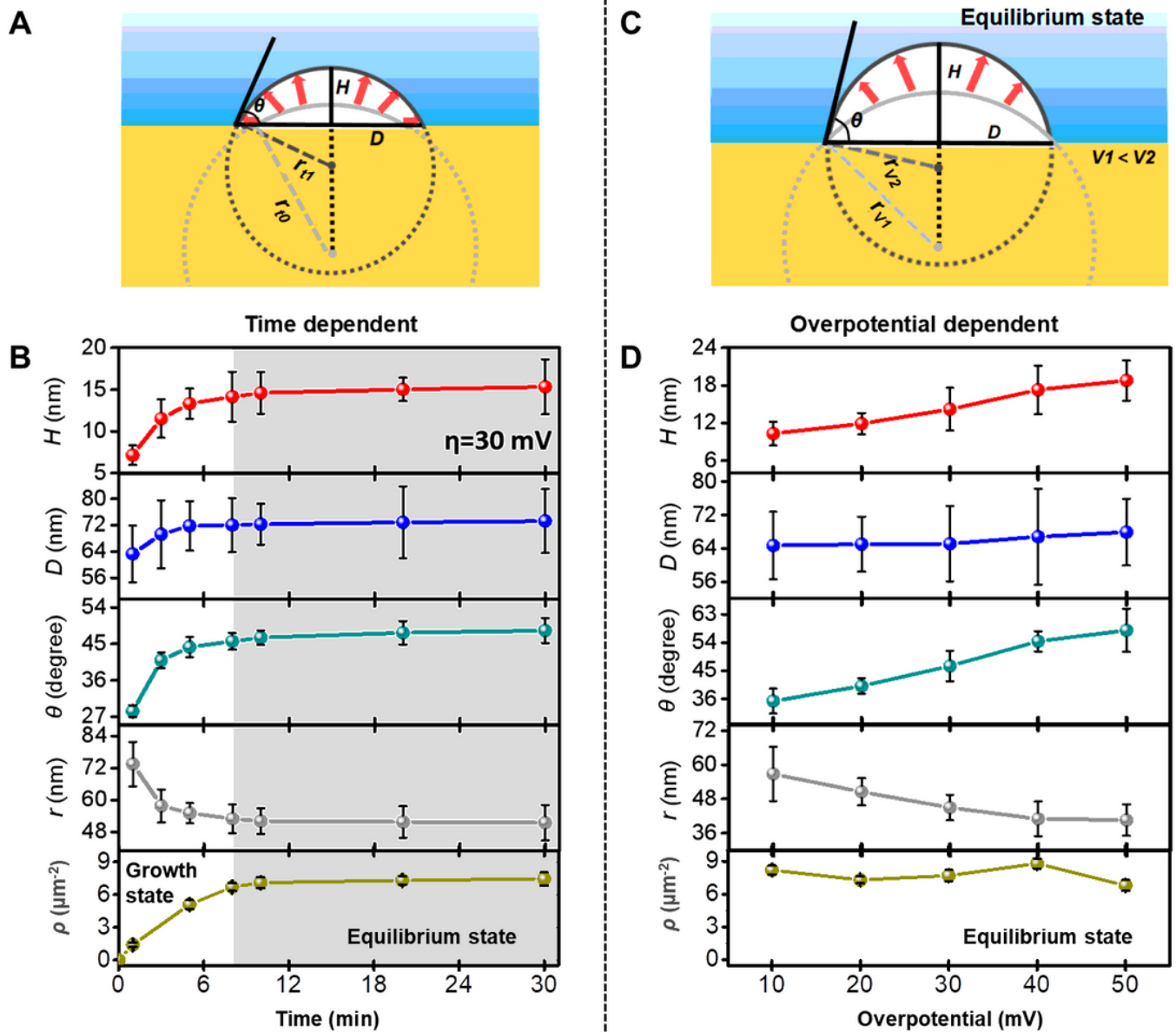
Figure 4

Time- and overpotential- dependent growth model of nanobubbles raised by analyses on AFM characterizations. **(A)** Schematic illustration of time-dependent growth model of nanobubbles. **(B)** Time-dependent variations of contact angle (θ), height (H), contact diameter (D), curvature radius (r) and number density (ρ) of NBs at 30 mV. **(C)** Schematic illustration of overpotential- dependent growth model of nanobubbles. **(D)** Overpotential-dependent variations of height (H), contact diameter (D), contact angle (θ) and curvature radius (r) and number density (ρ).
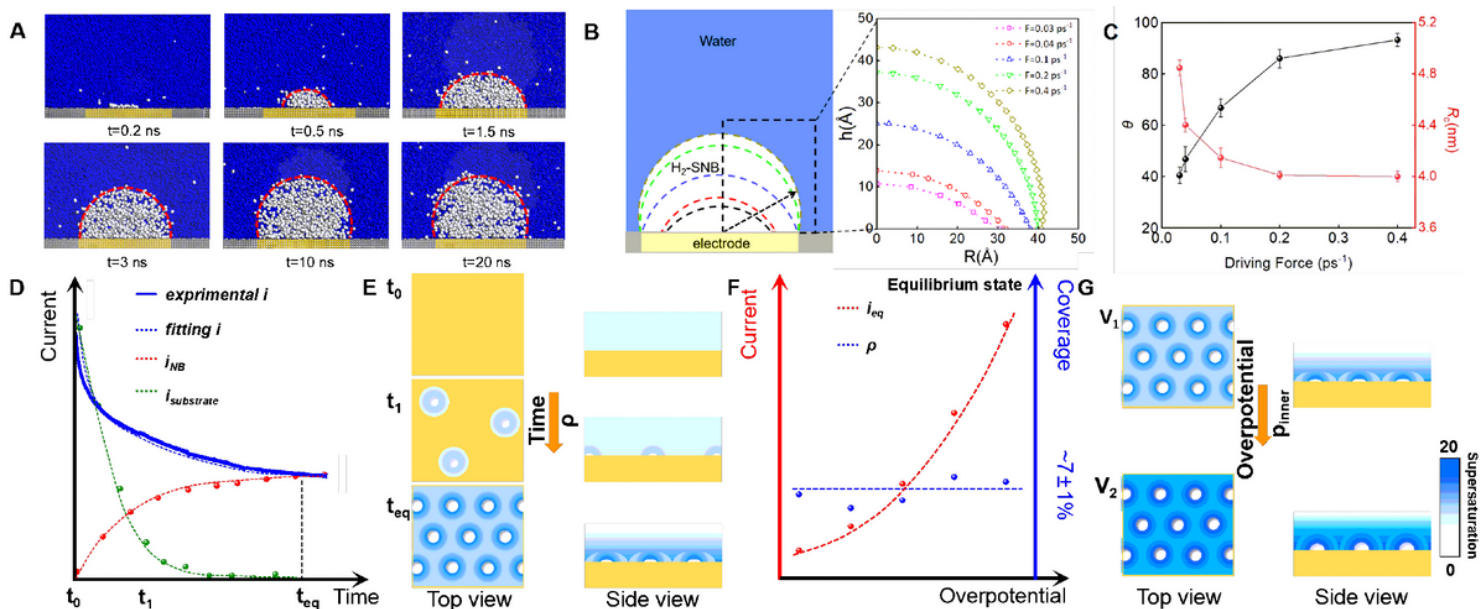
Figure 5

Simulations and electrochemical verification of interfacial H2 NBs. (A) Snapshots of the nucleation and growth of a H2NB on an electrode surface when the gas creation frequency F=0.4 ps-1. **(B)** Schematic diagram of the growth of a NB on Au electrode surface and the shape of NBs with different driving forces. **(C)** The contact angle of NB and curvature radius of NB corresponding to the different driving forces. **(D)** The time-dependent current variation of the diffusion, the free area and the sum of them. **(E)** Schematic illustration of time-dependent NB growth process at a certain overpotential. **(F)** Variation of coverage and equilibrium current at different overpotentials. **(G)** Schematic illustration of overpotential-dependent NB growth process.

Supplementary Files

This is a list of supplementary files associated with this preprint. Click to download.

- SI.docx